



# Electrophoretically self-assembled mixed metal oxide-TiO<sub>2</sub> nano-composite film structures for photoelectrochemical energy conversion: Probing of charge recombination and electron transport resistances

Nima Parsi Benehkohal\*, George P. Demopoulos\*

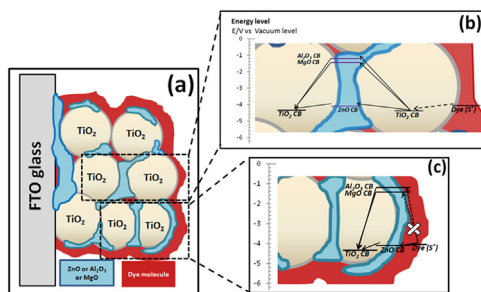
Department of Materials Engineering, McGill University, 3610 University Street, Montreal, QC H3A 2B2, Canada



## HIGHLIGHTS

- EPD construction of nanotitania/metal oxide composite films for DSSC application.
- In-situ metal oxide nanocoating of TiO<sub>2</sub> provides charge recombination resistance.
- TiO<sub>2</sub>–Al<sub>2</sub>O<sub>3</sub> nanocomposite film exhibits highest charge recombination resistance.
- TiO<sub>2</sub>–ZnO film exhibits least electron transport resistance and highest efficiency.
- Optimization of electronic properties of metal oxide with photovoltaic performance.

## GRAPHICAL ABSTRACT



## ARTICLE INFO

### Article history:

Received 19 December 2012

Received in revised form

11 April 2013

Accepted 12 April 2013

Available online 16 May 2013

### Keywords:

Electrophoretic deposition

Dye sensitized solar cell

Nanocomposite film

Electron transport

Charge recombination

Electrochemical impedance spectroscopy

## ABSTRACT

Nanotitania/metal oxide composite films are prepared via the coupling of low DC voltage Electrophoretic Deposition (EPD) of P25 TiO<sub>2</sub> nanoparticles with simultaneous electrolytic deposition of hydrous metal oxides, namely ZnO, MgO and Al<sub>2</sub>O<sub>3</sub>. The nanocomposite films are built into dye-sensitized solar cell photoanodes and their interfacial charge recombination and electronic resistances are investigated. The nano hydrous oxides were found to co-deposit (1–3 wt%) uniformly within the TiO<sub>2</sub> film (forming island-like nanodeposits) significantly increasing film adhesion. Analysis via Electrochemical Impedance Spectroscopy and Open Circuit Voltage Decay techniques found, among the three composite films, the TiO<sub>2</sub>–Al<sub>2</sub>O<sub>3</sub> electrode to exhibit the highest charge recombination resistance at the TiO<sub>2</sub>/electrolyte interface ( $R_{rec}$ ) and as consequence an increase in  $V_{oc}$ . However, its conversion efficiency (4.14%) was the lowest because it suffered from very high electron transport resistance ( $R_t$ ) in the TiO<sub>2</sub> network. By comparison, the TiO<sub>2</sub>–MgO film resulted in 5.40% efficiency and the TiO<sub>2</sub>–ZnO film in 5.85% efficiency—both exhibiting significantly lower  $R_t$  resistance. The obtained results point to the need for simultaneous optimization of the nanocomposite TiO<sub>2</sub>/metal oxide film structure in terms of high interfacial charge recombination resistance and low overall electron transport resistance.

© 2013 Elsevier B.V. All rights reserved.

## 1. Introduction

The dye-sensitized solar cell (DSSC) is a unique photoelectrochemical energy conversion device, which since its first

\* Corresponding authors. Tel.: +1 5144358763; fax: +1 5143984492.

E-mail addresses: [Nima.parsibenehkohal@mail.mcgill.ca](mailto:Nima.parsibenehkohal@mail.mcgill.ca) (N. Parsi Benehkohal), [george.demopoulos@mcgill.ca](mailto:george.demopoulos@mcgill.ca) (G.P. Demopoulos).

introduction in 1991 [1] has attracted tremendous R&D attention. The DSSC is typically composed of a mesoporous nanocrystalline  $\text{TiO}_2$  film covered by a monolayer of dye molecules, electrolyte, and counter electrode. The structure of  $\text{TiO}_2$  photoanode provides a large surface area that enables abundant dye loading on the surface to maximize the amount of photogenerated charge. In addition to efficient light harvesting, a large electron diffusion length in  $\text{TiO}_2$  photoanode is necessary to obtain good collection efficiency. It is noted that unhindered charge transport in the  $\text{TiO}_2$  network accompanied by minimized interfacial charge recombination can lead to the large diffusion length.

There have been intensive studies on a range of fabrication procedures to modify the  $\text{TiO}_2$  photoelectrode by incorporating different composite films in order to enhance the cell conversion efficiency. Some studies constructed the composite photoanode based on a mixture of nanoparticles with different size, shape such as, nanotube and nanowire, which resulted in enhanced conversion efficiency due to the facile electron transport as well as light scattering [2–4]. Moreover, different metal oxides have been investigated as scattering layer on top of the transparent  $\text{TiO}_2$  film such as  $\text{ZrO}_2$  [5] and  $\text{Al}_2\text{O}_3$  [6]. Another approach in fabrication of composite photoanodes is the coating of the transparent  $\text{TiO}_2$  film with a thin layer of another metal oxide (a type of core–shell configuration applied to the whole film as opposed the individual particles). This approach has been reported to enhance the cell performance of DSSCs by retarding interfacial recombination. As overcoat materials, different metal oxides with higher conduction band (CB) edges, e.g.,  $\text{MgO}$ ,  $\text{ZnO}$ ,  $\text{Nb}_2\text{O}_5$ ,  $\text{Al}_2\text{O}_3$ ,  $\text{SiO}_2$ , and  $\text{ZrO}_2$ , are selected in order to minimize the back transfer of photoinjected electrons through the  $\text{TiO}_2$ /dye/electrolyte interface and, hence, improve the  $V_{\text{oc}}$  and subsequently cell efficiency [7–17]. Furthermore, overcoating with different metal hydroxides such as  $\text{Mg}(\text{OH})_2$ ,  $\text{Zn}(\text{OH})_2$ ,  $\text{Al}(\text{OH})_3$ , and  $\text{La}(\text{OH})_3$  prepared by electrodeposition has also been reported [18,19]. It is worth noting that different metal hydroxides with more negative CB compared to that of  $\text{TiO}_2$  (−4.21 eV vs. vacuum scale [20]) were also applied as a blocking  $\text{TiO}_2$  layer at the FTO/ $\text{TiO}_2$  interface in order to decrease electron leakage from the substrate to electrolyte [21–23].

In the present work, given that the majority of previous works have focused on the core–shell (overcoat) composite structure, we have decided to fabricate and study the photovoltaic behavior of an alternative self-assembled co-deposited mixed metal oxide film. We call this film geometry, hybrid or mixed composite structure. There are a few previous studies with which the new mixed composite structure can be related. Thus Chou et al. [24] reported the fabrication of a  $\text{TiO}_2/\text{NiO}$  mixed composite film by mixing the Ni powder with  $\text{TiO}_2$  particles, and depositing it on FTO-glass substrate via the spin coating process; the cell employing the composite structure yielded a better conversion efficiency ( $\eta \sim 3.80\%$ ) than that of the conventional  $\text{TiO}_2$  film-based DSSC (3.27%). This improvement was attributed to the blocking effect of the NiO particles. Moreover, Niu et al. [25] demonstrated that mixed  $\text{TiO}_2$ – $\text{SiO}_2$  composite electrodes led to pronounced increase in  $\eta$  from  $\sim 5.8\%$  (bare  $\text{TiO}_2$ ) to  $\sim 8.4\%$ . This increase was explained in terms of the favorable effect  $\text{SiO}_2$  particles had on the dispersion of  $\text{TiO}_2$ , as well as on its role as blocking layer against charge recombination. However, Chappel et al. [26] claimed that the core–shell film structure is preferable as they argued the metal oxide (usually with more negative CB compared to  $\text{TiO}_2$ ; distributed in the entire film of the mixed structure) will act as energy barriers to photoinjected electrons diffusing toward the current collector. However, this loss in charge transport depends on how far the CB position of the second metal oxide is located compared to  $\text{TiO}_2$ . In addition, in the core–shell (overcoat) film structure, dye molecules are adsorbed directly onto the co-deposited shell and

not  $\text{TiO}_2$ . As a result, not only the amount of dye loading can be affected depending on shell's surface properties (IEP-iso electric point) [15], but also owing to the higher CB edge of the shell oxide, electron injection into  $\text{TiO}_2$  can be hindered in agreement to [10,19,27]. This issue motivated us to investigate the photovoltaic properties of a hybrid/mixed metal oxide nanodeposit configuration that allows for effective interfacial charge recombination resistance without compromising photoelectron generation and injection achieved by direct dye loading on uncoated areas of  $\text{TiO}_2$  surface.

Recently, we showed a significant improvement in overall cell efficiency using a nanocomposite  $\text{TiO}_2$ – $\text{ZnO}$  electrode structure as compared to  $\text{TiO}_2$  alone [28]. Therefore, we decided to expand our study by considering  $\text{Mg}(\text{NO}_3)_2$  and  $\text{AlCl}_3$  in addition to  $\text{Zn}(\text{NO}_3)_2$  as charging agents, prepare three mixed ( $\text{TiO}_2$ – $\text{MO}_x$ ) composite films, probe their charge recombination and electron transport properties and relate ultimately film structure to device performance. To this end self-assembled composite electrode films are constructed via our recently developed aqueous suspension-based EPD method [29] and after characterization they are analyzed by electrochemical impedance spectroscopy (EIS), incident photon current conversion efficiency (IPCE) and open circuit voltage decay (OCVD) techniques.

## 2. Experimental

### 2.1. Aqueous suspension preparation and EPD procedure

An aqueous suspension was prepared as optimized in our previous work [29]. The suspension consisted of 5% v/v de-ionized water–isopropanol and 5 g  $\text{L}^{-1}$  of  $\text{TiO}_2$  powder (AEROXIDE®  $\text{TiO}_2$  P25, Evonic). In addition,  $10^{-3}$  M of 3 different salts namely,  $\text{Zn}(\text{NO}_3)_2$ ,  $\text{Mg}(\text{NO}_3)_2$ , and  $\text{AlCl}_3$  were added act as charging and binder (upon electrolytic deposition) agents. The suspension was first mixed for 75 min with a magnetic stirrer and after for 15 min with an ultrasonic stirrer prior to EPD. The zeta potential and suspension conductivity were measured with a Malvern Zetasizer Nano ZS (Malvern Instruments) and an Oakton conductivity meter, respectively. In order to perform EPD, constant current density (0.1–0.3 mA  $\text{cm}^{-2}$ ) was applied between a stainless steel sheet (anode) and a fluorine-doped tin-oxide conducting glass substrate (FTO-Glass, 7  $\Omega \text{ cm}^{-2}$ , Nippon Sheet Glass, Japan). This current density range was used in order to minimize water decomposition by applying low voltage ( $\sim 2.2$ –4.2 V) between two electrodes [29]. The deposition area of the electrode was  $5 \text{ cm}^2$ . The distance between the two electrodes was 2 cm. The deposition was performed for different times over the range of 5–15 min using a Keithley 2400 Source Meter as a power supply. After deposition, the mixed composite films were dried at room temperature and subjected to annealing at 450 °C in air for 30 min [30].

### 2.2. Characterization of mixed nano-composite films

The thickness and roughness of the three composite films (no separate scattering layer was applied) were measured using the Dektak 3030 surface profiler system (Veeco Instruments Inc., U.S.A.). The morphology of the  $\text{TiO}_2$  films was characterized by a cold-FEG-SEM Hitachi SU-8000. Energy-dispersive X-ray spectroscopy (Oxford, SU-8000 Hitachi) was also employed to determine the chemical species of the composite substrates. High resolution Transmission Electron Microscopy (HR-TEM) images were obtained using a Philips CM-200 microscope operating at 200 kV. X-ray diffraction (XRD) analysis was performed using a Bruker D8 diffractometer equipped with a GADDS 2D detector and  $\text{Cu K}\alpha$  radiation ( $\lambda = 0.15406 \text{ nm}$ ) at a scan rate of 5°/min. X-ray

**Table 1**

Properties of different suspensions and deposited mixed composite films.

Charging agent	Zeta potential (mV)	Suspension pH	Suspension conductivity ( $10^{-6}$ S cm $^{-1}$ )	Applied current density for EPD (mA cm $^{-2}$ ) – applied voltage (V)	Film roughness after annealing (Å)	Film composition after annealing	Metal oxide film content (wt.%)
AlCl <sub>3</sub>	35 ± 1.0	3.3	395	0.3 (2.6–3.7 V)	6475 ± 1006	TiO <sub>2</sub> –Al <sub>2</sub> O <sub>3</sub>	1.66 ± 0.03
Zn(NO <sub>3</sub> ) <sub>2</sub>	31 ± 3.0	4.2	213	0.1 (2.2–3.2 V)	4593 ± 1621	TiO <sub>2</sub> –ZnO	2.39 ± 0.09
Mg(NO <sub>3</sub> ) <sub>2</sub>	20 ± 1.5	4.2	216	0.3 (3.5–4.2 V)	13,425 ± 3058	TiO <sub>2</sub> –MgO	1.07 ± 0.01

photoelectron spectroscopy (XPS) measurement was performed and collected with a Thermo Scientific KAlpha instrument, using an Al K $\alpha$  X-ray source at 1486.6 eV. Spectra were generated at a perpendicular takeoff angle, using a pass energy of 20 eV and steps of 0.1 eV. During analysis, the pressure was in the order of  $\sim 10^{-10}$  Torr. Ar $^+$  ion bombardment with energy of 2 keV for 30 s was carried out prior to collecting the spectra in order to remove any charging effects from carbon-based contaminants. As an internal reference for the absolute binding energies, the Au (4f<sub>7/2</sub>) peak was used. The experimental spectra were de-convoluted after subtraction of the Shirley background using the VG Avantage program. In order to determine the weight percentage of metallic oxide content of the TiO<sub>2</sub> deposited film, the magnesium and zinc were dissolved (24 h) in acidic (2 M HCl) and aluminum in basic (5 N NaOH) solution. Then, they were analyzed by atomic absorption (AA) using a Varian Atomic Absorption spectrometer.

### 2.3. Cell fabrication and photo-electrochemical measurements

After annealing, the TiO<sub>2</sub>–Mo<sub>x</sub> films were sensitized by immersion into a room temperature 0.5 mM ethanol solution of N719 for 48 h. The composite films were rinsed with ethanol to remove physisorbed dye molecules. The absorption spectra of dye-loaded films were recorded by UV/vis spectrophotometry (Lambda20, PerkinElmer). As a counter electrode, a Pt layer was prepared by spreading one drop of 5 mM H<sub>2</sub>PtCl<sub>6</sub> solution (iso-propanol), air dry, and then heating at 380 °C for 30 min. The working and counter electrodes were assembled into a sandwich-type cell and sealed with a thermoplastic sealant of 30  $\mu$ m thickness (Surlyn®-30, Dyesol) by hot-pressing, followed by insertion of commercial

electrolyte solution (composition: I<sub>3</sub><sup>-</sup>/I<sup>-</sup>, organic iodide salt, pyridine derivative, acetonitrile and valeronitrile; EL-HPE; Dyesol) through a hole on the Pt electrode.

Current–voltage ( $I$ – $V$ ) curves were recorded using a solar simulator of class ABA (PV Measurements Inc., Model IV 10) under illumination of uniform light approximating 100 mW cm $^{-2}$  (AM 1.5 solar emission) provided by a Xenon lamp. The light intensity was adjusted with a Si reference cell. Duplicate measurements with each type of DSSC were made to ensure reproducible results. The IPCE measurements were performed with a PV Measurements Inc. Quantum Efficiency system, model QEX10, using a 150 W Xe lamp coupled with a slit monochromator. The intensity of incident monochromatic light was calibrated with a Si photodiode. The electrochemical impedance spectra (EIS) and open-circuit voltage decay (OCVD) analysis were measured by using a VSP-potentiostat system (BioLogic). EIS was carried out under 100 mW cm $^{-2}$  illumination, applying a 10 mV AC signal and scanning in a frequency range between 400 kHz and 1 Hz at different forward applied bias. The EIS data were analyzed with the Z-View software. OCVD analysis [31–33] was carried out to provide detailed curves of electron lifetime ( $\tau$ ) versus open circuit voltage ( $V_{oc}$ ). In this measurement, cells were illuminated and the decay of  $V_{oc}$  was studied as a function of time after the switch-off of the light.

## 3. Results and discussion

### 3.1. Characterization of aqueous suspension and the nanocomposite films

As described before, the same 10 $^{-3}$  M concentration of three different salts, namely AlCl<sub>3</sub>, Zn(NO<sub>3</sub>)<sub>2</sub>, and Mg(NO<sub>3</sub>)<sub>2</sub>, was added to

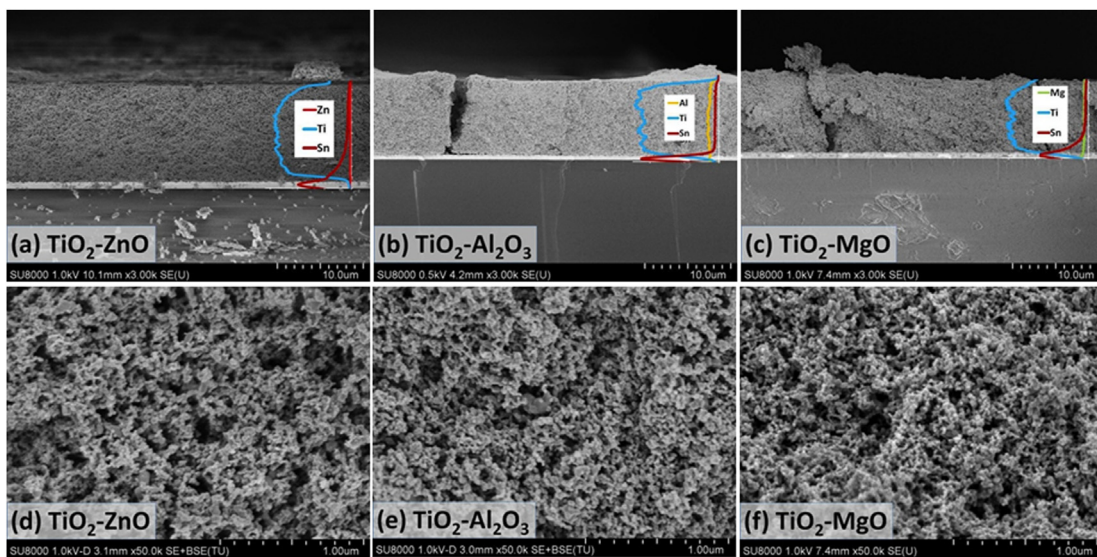


**Fig. 1.** (a), (b), and (c) Cross section SEM images of annealed composite films. (c), (d), and (e) high magnification top-view film images. Insets in (a), (b), and (c) show the EDS line scan of the film cross section.

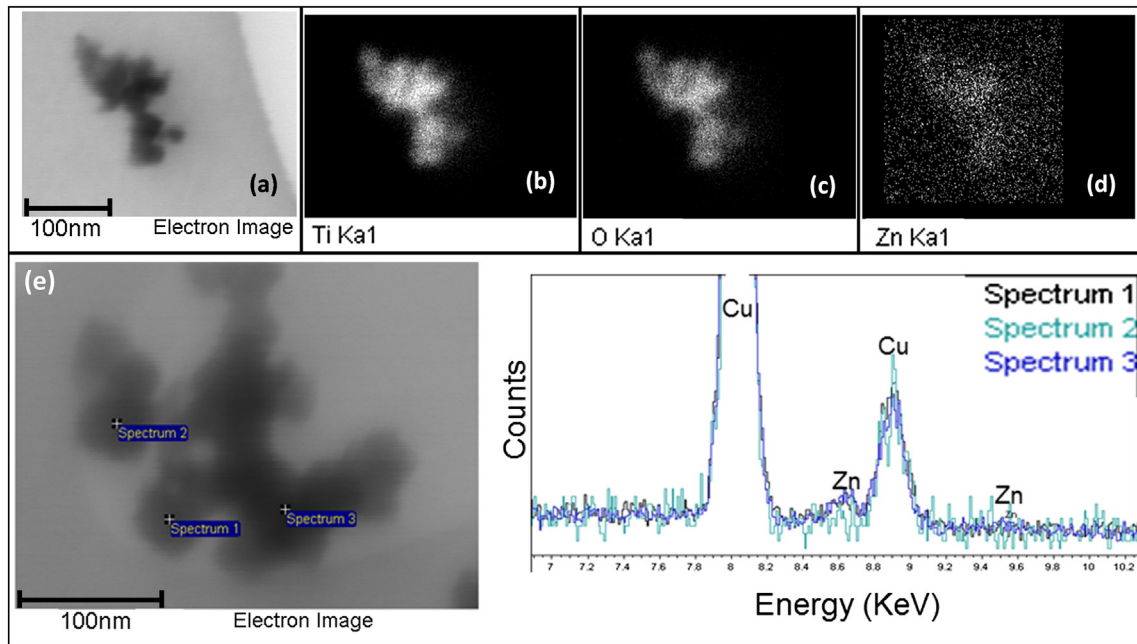


**Fig. 2.** Elemental maps of part of  $\text{TiO}_2$ – $\text{ZnO}$  film in high magnification. (a) STEM image of nanoparticles of  $\text{TiO}_2$ – $\text{ZnO}$  composite film. (b), (c), (d) Elemental maps displaying Ti, O and Zn distribution, and (e) EDS spot analysis on some particles removed from the  $\text{TiO}_2$ – $\text{ZnO}$  film.

the 5% v/v water–isopropanol mixture. As indicated in Table 1,  $\text{AlCl}_3$  provided the most stable suspension verified by the highest zeta potential at 35 mV. Despite the higher zeta potential that is considered advantageous for EPD, the higher suspension conductivity is not desirable since the free ions tend to carry the bulk of the charge and not the charged particles. On the other hand,  $\text{Mg}(\text{NO}_3)_2$  resulted in the lowest zeta potential and consequently least stable suspension probably due to its lower tendency to be specifically adsorbed on the surface of  $\text{TiO}_2$  particles, however the suspension was still stable enough against sedimentation for EPD to take place.

Constant current density EPD was performed at  $0.1 \text{ mA cm}^{-2}$  for the suspension containing  $\text{Zn}(\text{NO}_3)_2$  and at  $0.3 \text{ mA cm}^{-2}$  for the other two suspensions. These values were determined experimentally to be the highest possible current density that will allow deposition of continuous and uniform films at a potential below the threshold of water decomposition. The present system does not rely on very high applied voltage that is commonly used in organic media to ensure film adhesion but rather on co-deposition of hydrous metal oxide [29].

As can be deduced from the SEM images shown in Fig. 1, EPD has led to the formation of robust films. It is evident that the  $\text{TiO}_2$ – $\text{ZnO}$  and  $\text{TiO}_2$ – $\text{Al}_2\text{O}_3$  films exhibit superior quality and uniformity compared to the  $\text{TiO}_2$ – $\text{MgO}$  film. This observation is in agreement with the roughness values measured by surface profilometry (Table 1). Apparently the lower zeta potential of the  $\text{Mg}(\text{NO}_3)_2$  suspension caused formation of large size aggregates and consequently rougher surface. Moreover, the high magnification SEM images of these films shown in Fig. 1(d)–(f) provide clear evidence of a well developed mesoporous structure, which is required for efficient dye loading and electrolyte diffusion in DSSC application.

The deposition mechanism of a mixed  $\text{TiO}_2$ – $\text{ZnO}$  composite film was described in detail in our previous study [29]. In short, during EPD due to cathodic reduction of  $\text{H}^+$  and nitrate ions, the local pH increases leading to electrolytic deposition of hydrous metal oxide that acts as binder for the physically deposited  $\text{TiO}_2$  particles, hence promoting the building of an adhesive film. Chemical analysis of the deposited films (shown in Table 1), as well as EDS analysis performed on the film cross sections (shown in Fig. 1), confirmed the

uniform co-deposition of zinc, magnesium and aluminum oxide at an amount less than 3%, independent of the deposition time.

In order to further investigate the mode of metal oxide co-deposition during EPD of  $\text{TiO}_2$ , elemental maps of some particles removed from the  $\text{TiO}_2$ – $\text{ZnO}$  film were examined at very high magnification (Fig. 2). As it can be seen, zinc was deposited on the surface of  $\text{TiO}_2$  particles uniformly as nanodots rather than as a continuous shell, apparently due to its small quantity. Furthermore, EDS spot analysis on some particles from the same film (Fig. 2(e)) confirmed that zinc oxide was present in various spots of the particle surface (e.g. points 1 and 3) but not on other spots (e.g. point 2). According to the XRD results (Figure S1, Supporting

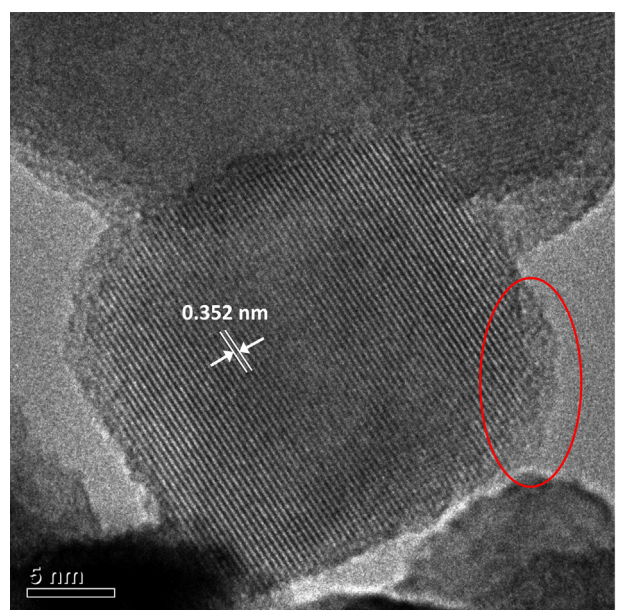


**Fig. 3.** HR-TEM image of  $\text{TiO}_2$ – $\text{ZnO}$  composite film showing a single  $\text{TiO}_2$  nanoparticle (characteristic lattice spacing of 0.35 nm corresponding to (101) planes in anatase) that appears partially coated with  $\text{ZnO}$  ( $\sim 1 \text{ nm}$  surface deposit).

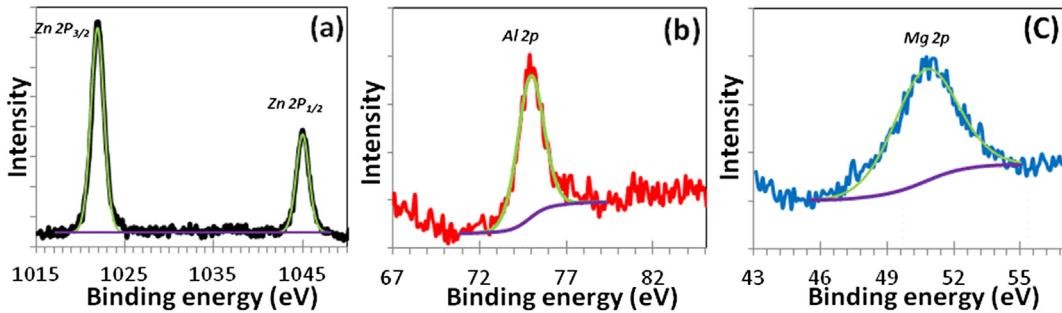


Fig. 4. High resolution XPS spectra of (a) Zn 2p region, (b) Al 2p region, and (c) Mg 2p region for annealed  $\text{TiO}_2$ –ZnO,  $\text{TiO}_2$ – $\text{Al}_2\text{O}_3$ , and  $\text{TiO}_2$ –MgO films, respectively.

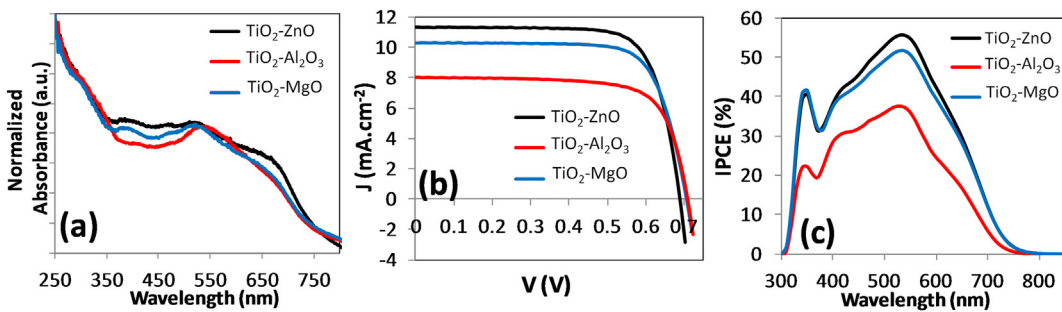


Fig. 5. (a) Absorption spectra of dye-covered nanocomposite film, (b)  $I$ – $V$  curves and (c) IPCE of various DSSCs prepared by different nanocomposite photoanodes.

Information), all three annealed composite films showed only the mixed phase  $\text{TiO}_2$  (anatase and rutile, since the commercial  $\text{TiO}_2$  powder (P25) used in our work is composed of anatase and rutile [34]) and FTO glass. ZnO,  $\text{Al}_2\text{O}_3$ , and MgO were not detected by XRD most likely due to their small quantity (<3%) as also noted elsewhere [35,36]. It is notable that there was no sign of  $\text{Zn}^{2+}$ ,  $\text{Mg}^{2+}$ , and  $\text{Al}^{3+}$  ions substitution into the  $\text{TiO}_2$  lattice as deduced from the lack of any XRD peak shift [37,38]. The absence of substitution was also deduced from High-resolution TEM analysis as per image presented in Fig. 3, where the characteristic lattice spacing of undoped anatase (0.352 nm) for (101) plane [39] is present. The same HR-TEM image of Fig. 3 further provides evidence of partial coating of the  $\text{TiO}_2$  surface by a nanodeposit (~1 nm thick rim). Therefore, ZnO,  $\text{Al}_2\text{O}_3$ , and MgO crystallites are considered to have deposited on the surface of  $\text{TiO}_2$  nanoparticles.

Finally, in order to positively substantiate the presence of co-deposited metal oxides XPS analysis was performed and presented in Fig. 4. The XPS high-resolution spectra exhibited peaks at 1021.93, 74.96, and 50.6 eV attributed to Zn 2p<sub>3/2</sub>, Al 2p, and Mg 2p states, which are characteristic of ZnO [40],  $\text{Al}_2\text{O}_3$  [41,42], and MgO [43–45], respectively.

### 3.2. Photo-electrochemical characterization

Before assembling the DSSC, UV–vis absorption spectra for dye-loaded films were measured and presented in Fig. 5(a). The differences in absorption spectra of these films are negligible

indicating that the co-deposited oxides did not alter the dye-adsorption properties of  $\text{TiO}_2$  (P25) – the main component of the sensitized film. Eventually, DSSCs were assembled using these three mixed composite films as photoanodes with similar thickness of ca. 11.5  $\mu\text{m}$ .  $I$ – $V$  measurements made on the cells, shown in Fig. 5(b) and Table 2, indicated that the  $\text{TiO}_2$ –ZnO photoanode produced the highest short circuit current density ( $J_{\text{sc}}$ ) and conversion efficiency ( $\eta$ ) almost 40% higher than that of the  $\text{TiO}_2$ – $\text{Al}_2\text{O}_3$  film that showed the lowest performance.

Measurements of IPCE, which is defined as the number of electrons generated by light in the external circuit divided by the number of incident photons, of the three composite photoanodes are shown in Fig. 5(c). The maximum IPCE value for the three composite films at ~530 nm decreases from 55.7, to 51.6, to 37.6% in direct correspondence with the observed drop of  $J_{\text{sc}}$  from 11.3, to 10.3, to 8.03  $\text{mA cm}^{-2}$  for  $\text{TiO}_2$ –ZnO,  $\text{TiO}_2$ –MgO, and  $\text{TiO}_2$ – $\text{Al}_2\text{O}_3$ , respectively.

Electrochemical impedance spectroscopy (EIS) is regarded as a powerful tool for investigating the electron transport and kinetics of interfacial charge transfer processes in DSSCs [46]. A typical EIS spectrum for a DSSC exhibits three semicircles in the Nyquist plot (see Fig. 6(a)). The left (high frequency) arc represents ( $R_{\text{CE}}$ ), which consists of the charge transfer process at the Pt counter electrode/electrolyte ( $R_{\text{Pt}}$ ) and FTO/ $\text{TiO}_2$  interfaces ( $R_{\text{CO}}$ ); the central arc is related to charge transport resistance in  $\text{TiO}_2$  film ( $R_{\text{t}}$ ), recombination at the  $\text{TiO}_2$ /dye/electrolyte interfaces ( $R_{\text{rec}}$ ) and the chemical capacitance ( $C_{\mu}$ ); and the third arc is associated with electrolyte diffusion impedance ( $Z_{\text{w}}$ ) [47]. The third arc is not discernible here (Fig. 6(a)) because of overlap with the middle-frequency arc [48] probably due to the use of high performance commercial electrolyte with a small diffusion resistance. In this study we carried out EIS analysis at varying applied voltage in order to verify whether there is a shift in the CB of  $\text{TiO}_2$  (as a result of the metal oxide co-deposition) thus allowing for interpretation of  $R_{\text{rec}}$  differences. This CB displacement is observable from the  $C_{\mu}$  shift as reported

Table 2

Photovoltaic parameters of different DCCSs.

Film	$J_{\text{sc}}$ ( $\text{mA cm}^{-2}$ )	$V_{\text{oc}}$ (V)	Fill factor	$\eta_{\text{max}}$ (%)	$\eta_{\text{average}}$ (%)
$\text{TiO}_2$ –ZnO	11.3	689	0.75	5.86	5.57
$\text{TiO}_2$ –MgO	10.3	706	0.74	5.40	5.36
$\text{TiO}_2$ – $\text{Al}_2\text{O}_3$	8.03	710	0.72	4.14	3.84

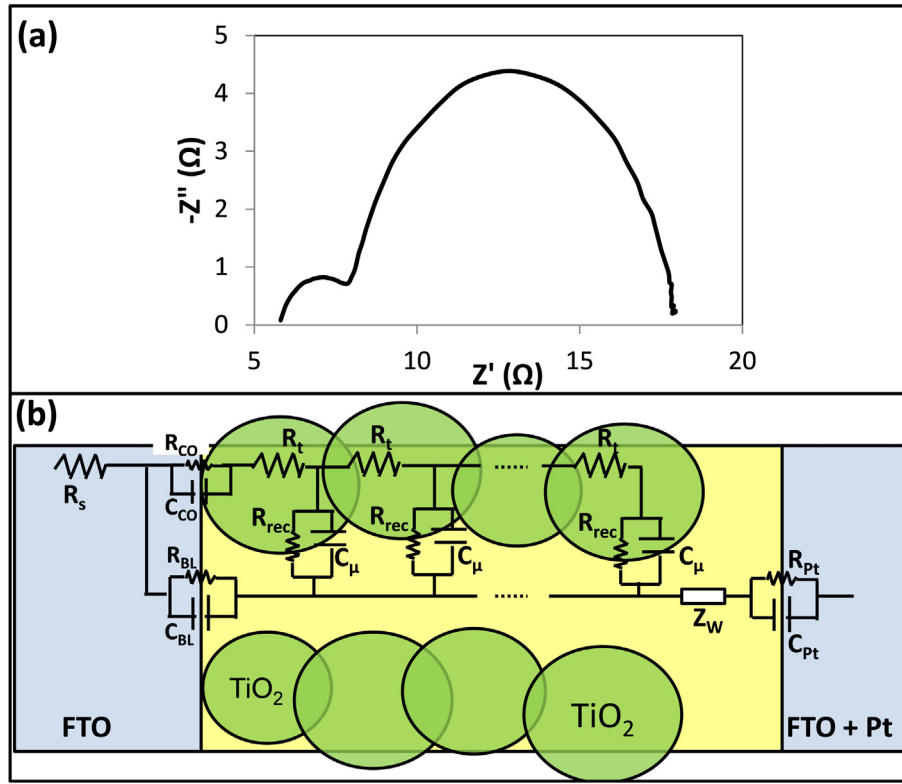


**Fig. 6.** (a) Typical Nyquist plots of DSSC based on TiO<sub>2</sub>–ZnO film and measured under 1 sun illumination and the  $V_{oc}$  condition. (b) General transmission line model of DSSCs [47]. The ( $R_{rec}$ ) is the charge recombination resistance at the TiO<sub>2</sub>/dye/electrolyte interface; ( $C_{\mu}$ ) is the chemical capacitance of the TiO<sub>2</sub> film; ( $R_t$ ) is the transport resistance of electrons in TiO<sub>2</sub> film; ( $Z_W$ ) is the Warburg element showing the Nernst diffusion of  $I^3^-$  in electrolyte; ( $R_{Pt}$ ) and ( $C_{Pt}$ ) are the charge-transfer resistance and double-layer capacitance at the platinumized counter electrode; ( $R_{BL}$ ) and ( $C_{BL}$ ) are the charge-transfer resistance and the corresponding double-layer capacitance at exposed FTO/electrolyte interface; ( $R_{co}$ ) and ( $C_{co}$ ) are the resistance and the capacitance at FTO/TiO<sub>2</sub> contact; ( $R_s$ ) is the series resistance, including the sheet resistance of FTO glass and contact resistance of the cell.

elsewhere [49]. All mentioned parameters were extracted from EIS measurements by employing the transmission model proposed by Fabregat-Santiago et al. [49–51] (see Fig. 6(b)) and plotted against the voltage drop at the sensitized electrode,  $V_F$ . The latter was obtained by subtracting the voltage drop of the series resistance ( $V_{series}$ ) from the applied potential ( $V_{app}$ ):  $V_F = V_{app} - V_{series}$  [49].  $V_F$  is proportional to the rise of the Fermi level of electrons in TiO<sub>2</sub>,  $V_F = (E_{Fn} - E_{F0})/q$ , where  $q$  is the positive elementary charge and  $E_{Fn}$  and  $E_{F0}$  are the electron Fermi level and the electron Fermi level at equilibrium, respectively. As shown in Fig. 7(b), the  $C_{\mu}$  of the three composite films did not shift indicating similar CB position.

Moreover, knowing the value of  $L$  (film thickness),  $R_{rec}$  and  $R_t$ , makes it possible to calculate important electron parameter called effective diffusion length ( $L_n$ ), using the following equation [52]:

$$L_n = L\sqrt{R_{rec}/R_t} \quad (1)$$

We further probed our cells via the use of OCVD, a complementary to EIS technique that provides very detailed curves of electron lifetime ( $\tau_n$ ) in DSSC devices as a measure of recombination kinetics [53]. It monitors the decay of photovoltage ( $V_{oc}$ ) after turning off the illumination [33]. The photovoltage decay reflects the decrease of electron concentration at the TiO<sub>2</sub>, which is mainly caused by charge recombination. As reported before [54], the electron lifetime ( $\tau$ ) can be derived from the rate of  $V_{oc}$  decay according to Eq. (2):

$$\tau = -\frac{k_B T}{e} \left( \frac{dV_{oc}}{dt} \right)^{-1} \quad (2)$$

where  $k_B$  is the Boltzmann constant,  $T$  is the temperature, and  $e$  is the electron charge. The calculated response times  $\tau$  as a function of  $V_{oc}$  for the three different DSSCs are displayed in Fig. 7(a) indicating highest and lowest electron lifetime for TiO<sub>2</sub>–Al<sub>2</sub>O<sub>3</sub> and TiO<sub>2</sub>–ZnO photoanodes, respectively.

### 3.3. Discussion

Now, the origin of performance differences in the three composite photoanodes will be discussed. As shown in Table 2, the  $V_{oc}$  was slightly improved from TiO<sub>2</sub>–ZnO to TiO<sub>2</sub>–MgO and TiO<sub>2</sub>–Al<sub>2</sub>O<sub>3</sub>. As we discussed in our previous study [28] and in agreement with Doh et al. [55]  $V_{oc}$  improvement can result from retardation of interfacial charge recombination (originating from ZnO, Al<sub>2</sub>O<sub>3</sub>, and MgO [22]) and/or from possible upward shift of the CB edge position of TiO<sub>2</sub> due to development of a dipole at the interface of TiO<sub>2</sub>/metal oxide [56–58]. However, since similar  $C_{\mu}$  values were determined (Fig. 7(b)) the CB edge for all 3 composite photoanodes, by extension is the same leaving retardation of charge recombination as the origin of the observed  $V_{oc}$  increase. According to Fig. 7(c), Al<sub>2</sub>O<sub>3</sub> presented the highest blocking ability for interfacial charge recombination because of its highest  $R_{rec}$ , which also resulted in the highest electron lifetime as determined from the OCVD measurements (Fig. 7(a)). The blocking ability of Al<sub>2</sub>O<sub>3</sub> is most likely due to its higher CB edge position (−1.31 eV vs. vacuum level) compared to MgO (−1.41 eV vs. vacuum level) and ZnO (−4.19 eV vs. vacuum level [15,20]). It is notable that the mechanism of charge transfer determining  $R_{rec}$  is via direct transfer from the TiO<sub>2</sub> CB [31]. However, electrons may recombine not only from the CB but also from localized intraband states as well as surface states in the band gap [50,59]. Therefore, it is also

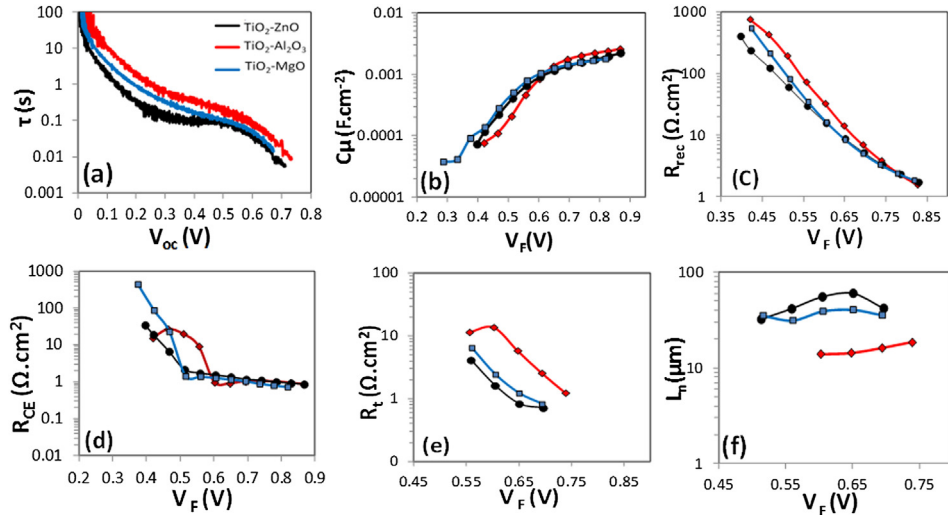


**Fig. 7.** (a) Electron lifetime ( $\tau$ ) as a function of  $V_{oc}$  for DSSCs based on different nano-composite photoanodes obtained from OCVD measurement. (b), (c), (d), (e), and (f) Impedance parameters of the various electrodes as function of the voltage drop,  $V_F$  (after series resistance correction).

interesting to probe the region of lower Fermi levels [54]. Thus, the OCVD technique was employed as it allows us to monitor the kinetics of recombination in the domain of low photovoltages [33,54]. It is apparent from the data of Fig. 7(a) that the composite films containing  $\text{Al}_2\text{O}_3$  and  $\text{MgO}$  exhibited more linear electron lifetime curves at lower voltage (below  $\sim 0.5$  V) than the film containing  $\text{ZnO}$ . This means that  $\text{Al}_2\text{O}_3$  and  $\text{MgO}$  offered better passivation of surface trap states in comparison to  $\text{ZnO}$ , a finding in good agreement with [31] where  $\text{Al}_2\text{O}_3$  was employed as an overcoat. However, as shown in Table 2,  $\text{TiO}_2\text{--Al}_2\text{O}_3$  photoanode yielded rather poor performance in terms of  $J_{sc}$  and  $\eta$  despite its higher charge recombination resistance. The observed lower  $J_{sc}$  and the corresponding lower IPCE of the  $\text{TiO}_2\text{--Al}_2\text{O}_3$  photoanode may be linked to a decrease in injection yield and/or charge collection efficiency. Since all three photoanodes had the same CB position of  $\text{TiO}_2$  as verified by EIS (Fig. 7(b)), and not a significant difference in the amount of dye loading as verified by the UV-vis

absorption spectra (Fig. 5(a)) charge injection efficiency from the excited dye to  $\text{TiO}_2$  must have been the same for all of them. Hence, it can be concluded that the collection/extraction efficiency of the injected electrons must be held responsible for the observed poor performance of the  $\text{TiO}_2\text{--Al}_2\text{O}_3$  electrode. The effective diffusion length ( $L_n$ ) of the photojected electron in a  $\text{TiO}_2$  film is very well known to be a good indicator for charge extraction [60]. According to Fig. 7(f), the  $L_n$  in  $\text{TiO}_2\text{--Al}_2\text{O}_3$  is much shorter than in the other photoanodes resulting in the lowest charge extraction, and consequently lowest  $J_{sc}$  and IPCE. This can be explained on the basis of  $\text{Al}_2\text{O}_3$ 's high CB position as schematically described in Fig. 8. It is postulated that photojected electrons cannot transport through the co-deposited metal oxide ( $\text{Al}_2\text{O}_3$ ) as its high CB acts as energy barrier in the contact point of two adjacent  $\text{TiO}_2$  particles. As a result  $R_t$  increases with the consequence of a shorter  $L_n$ . By comparison to  $\text{MgO}$  that has almost the same CB, it is possible that the blocking effect of  $\text{Al}_2\text{O}_3$  was more drastic due to

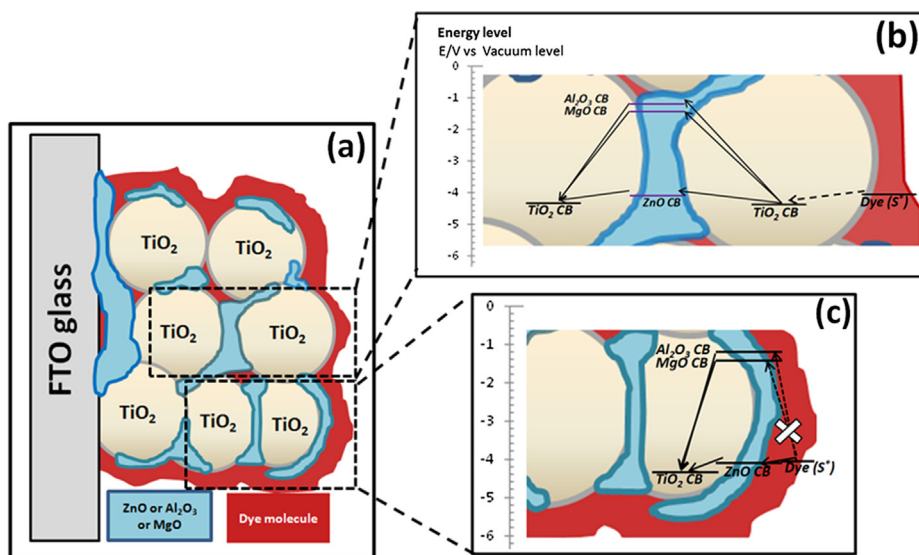


**Fig. 8.** (a) Schematic view of the mixed composite structure; (b) electron transfer inside the composite film in the case of the dye molecules been attached directly onto  $\text{TiO}_2$  particles; and (c) electron transfer inside the composite film in the case of the dye molecules been attached to the co-deposited metal oxide having higher CB band edge compared to that of  $\text{TiO}_2$ .

its ~55% higher amount (1.66 wt% vs. 1.07 wt% for MgO) that apparently resulted in a more insulating nanocoating in the TiO<sub>2</sub>–Al<sub>2</sub>O<sub>3</sub> electrode.

As mentioned above, in the mixed metal oxide composite structure, the co-deposited oxides do not form complete shell around the TiO<sub>2</sub> particles but give an island-like deposit on the TiO<sub>2</sub> surface similar to the schematic presented in Fig. 8. This structure can be considered advantageous in comparison to the core–shell structure in terms of sensitization and charge injection efficiency. In the latter structure, dye molecules are adsorbed directly onto the co-deposited shell and not TiO<sub>2</sub>. As a result, owing to the higher CB edge of the co-deposited oxide, electron injection into TiO<sub>2</sub> (Fig. 8(c)) is hindered in agreement to [10,19,27]. In contrast the island-like metal oxide co-deposition pattern makes some part of TiO<sub>2</sub> surface available for the direct dye adsorption and consequently direct charge injection into TiO<sub>2</sub> CB. Proper selection of the right co-deposited metal oxide that can match the electronic properties of TiO<sub>2</sub>, therefore, becomes critical in electrophoretically forming electrode structures with superior performance properties. In this regard ZnO is the co-deposited metal oxide of choice. Thus, a high conversion efficiency of 6.44% was obtained via multi-layer (by repeated cycles of EPD) construction of the transparent TiO<sub>2</sub>–ZnO film (8 layers) with optimum total thickness of 19 μm.

#### 4. Conclusion

Three different mixed oxide nanocomposite photoelectrodes, namely TiO<sub>2</sub>–ZnO, TiO<sub>2</sub>–Al<sub>2</sub>O<sub>3</sub> and TiO<sub>2</sub>–MgO were fabricated by low DC voltage EPD using a P25 nanotitania–isopropanol (5 vol.%) aqueous suspension. Co-deposition of secondary oxides was accomplished via in-situ cathodic electrolytic deposition of Zn, Mg, and Al hydroxides that acted as binders and finally converted to the oxide form upon annealing at 450 °C. Co-deposits of all three nano oxides were uniformly distributed (~1–3 wt%) within the film in island-like pattern on TiO<sub>2</sub> particle surfaces. As a result dye loading on the TiO<sub>2</sub> surface was not adversely affected. However, photovoltaic behavior was impacted in different ways by the electronic properties of the codeposited metal oxide. Thus among the three composite photoelectrodes, TiO<sub>2</sub>–Al<sub>2</sub>O<sub>3</sub> showed the highest charge recombination resistance at the TiO<sub>2</sub>/electrolyte interface ( $R_{\text{rec}}$ ) resulting in the highest electron lifetime and, consequently slightly higher  $V_{\text{oc}}$ . However, it showed the lowest conversion efficiency of 4.14% mainly due to the highest charge transport resistance ( $R_{\text{t}}$ ) of photojected electrons in the TiO<sub>2</sub> network arising from Al<sub>2</sub>O<sub>3</sub>'s high CB that acts as energy barrier compounded with a more insulating nanocoating. The TiO<sub>2</sub>–MgO film showed 5.40% conversion efficiency due to the lower  $R_{\text{t}}$  and longer  $L_{\text{n}}$  compared to TiO<sub>2</sub>–Al<sub>2</sub>O<sub>3</sub>. On the other hand, the TiO<sub>2</sub>–ZnO device showed the highest conversion efficiency (5.85%) and current density (11.3 mA cm<sup>−2</sup>) corresponding to the lowest  $R_{\text{t}}$ . The obtained results point to the need for simultaneous optimization of the nanocomposite TiO<sub>2</sub>/metal oxide film structure that delivers high interfacial charge recombination resistance while maintaining low the overall electron transport resistance.

#### Acknowledgments

This research is supported via a NSERC strategic project grant and sponsored by CIS Solar, Hydro-Quebec, Versatilis Inc and Targray Technology International. The authors are thankful to Professor Raynald Gauvin and Nicolas Brodusch for using the SEM Hitachi SU-8000. Furthermore, Professor N. Tufenki is thanked for permission to use the Zetasizer in her laboratory.

#### Appendix A. Supplementary data

Supplementary data associated with this article can be found online at <http://dx.doi.org/10.1016/j.jpowsour.2013.04.065>.

#### References

- [1] B. O'Regan, M. Grätzel, *Nature* 353 (1991) 737–740.
- [2] J. Yu, Q. Li, Z. Shu, *Electrochimica Acta* 56 (2011) 6293–6298.
- [3] Y.J. Kim, Y.H. Lee, M.H. Lee, H.J. Kim, J.H. Pan, G.I. Lim, Y.S. Choi, K. Kim, N.-G. Park, C. Lee, W.I. Lee, *Langmuir* 24 (2008) 13225–13230.
- [4] Y.-F. Chan, C.-C. Wang, B.-H. Chen, C.-Y. Chen, *Progress in Photovoltaics: Research and Applications* (2012). n/a–n/a.
- [5] S. Hore, C. Vetter, R. Kern, H. Smit, A. Hinsch, *Solar Energy Materials and Solar Cells* 90 (2006) 1176–1188.
- [6] K. Shin, Y. Jun, J.H. Moon, J.H. Park, *ACS Applied Materials & Interfaces* 2 (2009) 288–291.
- [7] K. Tennakone, J. Bandara, P.K.M. Bandaranayake, G.R.A. Kumara, A. Konno, *Japanese Journal of Applied Physics, Part 2: Letters* 40 (2001) L732–L734.
- [8] E. Palomares, J.N. Clifford, S.A. Haque, T. Lutz, J.R. Durrant, *Chemical Communications* (2002) 1464–1465.
- [9] E. Palomares, J.N. Clifford, S.A. Haque, T. Lutz, J.R. Durrant, *Journal of the American Chemical Society* 125 (2002) 475–482.
- [10] A. Kay, M. Grätzel, *Chemistry of Materials* 14 (2002) 2930–2935.
- [11] S.-S. Kim, J.-H. Yum, Y.-E. Sung, *Solar Energy Materials and Solar Cells* 79 (2003) 495–505.
- [12] T. Taguchi, X.-t. Zhang, I. Sutanto, K.-i. Tokuhiro, T.N. Rao, H. Watanabe, T. Nakamori, M. Uragami, A. Fujishima, *Chemical Communications* (2003) 2480–2481.
- [13] G.R.A. Kumara, M. Okuya, K. Murakami, S. Kaneko, V.V. Jayaweera, K. Tennakone, *Journal of Photochemistry and Photobiology A: Chemistry* 164 (2004) 183–185.
- [14] H.S. Jung, J.-K. Lee, M. Nastasi, S.-W. Lee, J.-Y. Kim, J.-S. Park, K.S. Hong, H. Shin, *Langmuir* 21 (2005) 10332–10335.
- [15] J. Kim, S. Lee, J. Noh, H. Jung, K. Hong, *Journal of Electroceramics* 23 (2009) 422–425.
- [16] C.-S. Chou, F.-C. Chou, J.-Y. Kang, *Powder Technology* 215–216 (2012) 38–45.
- [17] S.G. Chen, S. Chappel, Y. Diamant, A. Zaban, *Chemistry of Materials* 13 (2001) 4629–4634.
- [18] J.-H. Yum, S. Nakade, D.-Y. Kim, S. Yanagida, *The Journal of Physical Chemistry B* 110 (2006) 3215–3219.
- [19] T.A.N. Peiris, S. Senthilarasu, K.G.U. Wijayantha, *The Journal of Physical Chemistry C* 116 (2011) 1211–1218.
- [20] X. Yong, M.A.A. Schoonen, *American Mineralogist* 85 (2000) 543–556.
- [21] J. Xia, N. Masaki, K. Jiang, S. Yanagida, *The Journal of Physical Chemistry C* 111 (2007) 8092–8097.
- [22] Y. Liu, X. Sun, Q. Tai, H. Hu, B. Chen, N. Huang, B. Sebo, X.-z. Zhao, *Journal of Power Sources* 196 (2011) 475–481.
- [23] J.H. Noh, S. Lee, J.-Y. Kim, J.-K. Lee, H.S. Han, C.M. Cho, I.S. Cho, H.S. Jung, K.S. Hong, *The Journal of Physical Chemistry C* 113 (2008) 1083–1087.
- [24] C.-S. Chou, Y.-J. Lin, R.-Y. Yang, K.-H. Liu, *Advanced Powder Technology* 22 (2011) 31–42.
- [25] H. Niu, L. Liu, H. Wang, S. Zhang, Q. Ma, X. Mao, L. Wan, S. Miao, J. Xu, *Electrochimica Acta* 81 (2012) 246–253.
- [26] S. Chappel, S.-G. Chen, A. Zaban, *Langmuir* 18 (2002) 3336–3342.
- [27] H. Alarcón, M. Hedlund, E.M.J. Johansson, H. Rensmo, A. Hagfeldt, G. Boschloo, *The Journal of Physical Chemistry C* 111 (2007) 13267–13274.
- [28] N. Parsi Benehkoal, G.P. Demopoulos, *Journal of the Electrochemical Society* 159 (2012) B602–B610.
- [29] N. Parsi Benehkoal, M.A. Gomez, R. Gauvin, G.P. Demopoulos, *Electrochimica Acta* 87 (2013) 169–179.
- [30] K. Lee, C. Charbonneau, G. Shan, G. Demopoulos, R. Gauvin, *JOM Journal of the Minerals, Metals and Materials Society* 61 (2009) 52–57.
- [31] F. Fabregat-Santiago, J. Garcia-Canadas, E. Palomares, J.N. Clifford, S.A. Haque, J.R. Durrant, G. Garcia-Belmonte, J. Bisquert, *Journal of Applied Physics* 96 (2004) 6903–6907.
- [32] L. Grinis, S. Kotlyar, S. Rühle, J. Grinblat, A. Zaban, *Advanced Functional Materials* 20 (2010) 282–288.
- [33] J. Bisquert, A. Zaban, M. Greenshtein, I. Mora-Seró, *Journal of the American Chemical Society* 126 (2004) 13550–13559.
- [34] B. Erdem, R.A. Hunsicker, G.W. Simmons, E.D. Sudol, V.L. Dimonie, M.S. El-Aasser, *Langmuir* 17 (2001) 2664–2669.
- [35] Y. Ku, Y.-H. Huang, Y.-C. Chou, *Journal of Molecular Catalysis A: Chemical* 342–343 (2011) 18–22.
- [36] J.-J. Zou, B. Zhu, L. Wang, X. Zhang, Z. Mi, *Journal of Molecular Catalysis A: Chemical* 286 (2008) 63–69.
- [37] H. Wang, Z. Wu, Y. Liu, Z. Sheng, *Journal of Molecular Catalysis A: Chemical* 287 (2008) 176–181.
- [38] Z.-S. Wang, C.-H. Huang, Y.-Y. Huang, Y.-J. Hou, P.-H. Xie, B.-W. Zhang, H.-M. Cheng, *Chemistry of Materials* 13 (2001) 678–682.

[39] H. Zhang, P. Liu, F. Li, H. Liu, Y. Wang, S. Zhang, M. Guo, H. Cheng, H. Zhao, *Chemistry – A European Journal* 17 (2011) 5949–5957.

[40] L.S. Dake, D.R. Baer, J.M. Zachara, *Surface and Interface Analysis* 14 (1989) 71–75.

[41] W.M. Mullins, B.L. Averbach, *Surface Science* 206 (1988) 29–40.

[42] V. Di Castro, G. Polzonetti, G. Contini, C. Cozza, B. Paponetti, *Surface and Interface Analysis* 16 (1990) 571–574.

[43] S. Altieri, L.H. Tjeng, F.C. Voogt, T. Hibma, G.A. Sawatzky, *Physical Review B* 59 (1999) R2517–R2520.

[44] X.D. Peng, M.A. Bartea, *Surface Science* 233 (1990) 283–292.

[45] H.H. Huang, X. Jiang, Z. Zou, W.S. Chin, G.Q. Xu, W.L. Dai, K.N. Fan, J.F. Deng, *Surface Science* 412–413 (1998) 555–561.

[46] Q. Wang, J.-E. Moser, M. Gratzel, *The Journal of Physical Chemistry B* 109 (2005) 14945–14953.

[47] F. Fabregat-Santiago, J. Bisquert, E. Palomares, L. Otero, D. Kuang, S.M. Zakeeruddin, M. Gratzel, *The Journal of Physical Chemistry C* 111 (2007) 6550–6560.

[48] Z.-S. Wang, Y. Cui, Y. Dan-oh, C. Kasada, A. Shinpo, K. Hara, *The Journal of Physical Chemistry C* 111 (2007) 7224–7230.

[49] F. Fabregat-Santiago, G. Garcia-Belmonte, I. Mora-Sero, J. Bisquert, *Physical Chemistry Chemical Physics* 13 (2011) 9083–9118.

[50] F. Fabregat-Santiago, J. Bisquert, G. Garcia-Belmonte, G. Boschloo, A. Hagfeldt, *Solar Energy Materials and Solar Cells* 87 (2005) 117–131.

[51] V. Gonzalez-Pedro, X. Xu, I.n. Mora-Sero, J. Bisquert, *ACS Nano* 4 (2010) 5783–5790.

[52] J. Bisquert, I.n. Mora-Sero, *The Journal of Physical Chemistry Letters* 1 (2009) 450–456.

[53] J. Bisquert, F. Fabregat-Santiago, I.n. Mora-Sero, G. Garcia-Belmonte, S. Gimenez, *The Journal of Physical Chemistry C* 113 (2009) 17278–17290.

[54] A. Zaban, M. Greenstein, J. Bisquert, *ChemPhysChem* 4 (2003) 859–864.

[55] J.-G. Doh, J.S. Hong, R. Vittal, M.G. Kang, N.-G. Park, K.-J. Kim, *Chemistry of Materials* 16 (2003) 493–497.

[56] M. Law, L.E. Greene, A. Radenovic, T. Kuykendall, J. Liphardt, P. Yang, *The Journal of Physical Chemistry B* 110 (2006) 22652–22663.

[57] M.A. Butler, D.S. Ginley, *Journal of the Electrochemical Society* 125 (1978) 228–232.

[58] Y. Diamant, S. Chappel, S.G. Chen, O. Melamed, A. Zaban, *Coordination Chemistry Reviews* 248 (2004) 1271–1276.

[59] J. Bisquert, *The Journal of Physical Chemistry B* 108 (2004) 2323–2332.

[60] Q. Wang, S. Ito, M. Gratzel, F. Fabregat-Santiago, I. Mora-Sero, J. Bisquert, T. Bessho, H. Imai, *The Journal of Physical Chemistry B* 110 (2006) 25210–25221.